# Sub-minute in situ Fracture Test in a Lab CT-scanner

Clément Jailin, Amine Bouterf, Rafael Vargas, François Hild, Stéphane Roux

**IMMI manuscript No.**
(will be inserted by the editor)

# Sub-minute *in situ* Fracture Test in a Lab CT-scanner

**Clément Jailin · Amine Bouterf · Rafael Vargas · François Hild · Stéphane Roux**

Received: date / Accepted: date

**Abstract** The present study aims at demonstrating the feasibility of performing a fracture test in less than one minute in a lab CT scanner despite the severe time constraints of tomography acquisition. After introducing the basic concepts of Projection-based Digital Volume Correlation (P-DVC), the specific implementation of this methodology to a wedge splitting test on a refractory material is presented. The kinematics of the test is described over a mesh tailored to the sample geometry, and the elastic behavior of the sample is exploited through finite element computations to provide sensitivity fields of experimental boundary conditions to allow for their "measurements." Enhancing the simulation to account for crack advance with extended finite element analyses allows the sensitivity of the procedure to the crack position to be assessed. A confidence interval for the refractory toughness is finally obtained.

**Keywords** Castable refractory · Digital volume correlation · extended finite element analyses · Fracture energy · Wedge splitting test

## 1 Introduction

Computed Tomography (CT) has become a tool of choice in materials science [24, 32, 34]. Industrial or natural materials are imaged internally using lab tomographs or beamlines in synchrotron radiation facilities [2, 12]. Various microstructures are visualized and quantified in nondestructive or minimally intrusive ways [34, 26]. Further advances have been achieved by performing *in situ* mechanical tests [14, 4, 8, 7], and displacement measurements via Digital Volume Correlation (DVC [4,

Clément Jailin · Amine Bouterf · François Hild · Stéphane Roux
LMT, (ENS Paris-Saclay / CNRS / Univ. Paris-Saclay),
61 avenue du Président Wilson, F-94235 Cachan, France
E-mail: stephane.roux@ens-paris-saclay.fr

Rafael Vargas
Federal University of São Carlos (UFSCar),
Graduate Program in Materials Science and Engineering,
Rodovia Washington Luìs, km 235, 13565-905 São Carlos-SP, Brazil

33]). The latter technique has led to significant achievements in the mechanics of materials field [3,9].

One limitation of X-ray tomography with standard lab scale equipment is related to the acquisition time of the series of radiographs needed for 3D reconstructions. Tens of minutes if not hours are required for a single high quality reconstruction. Yet, many states are to be imaged to precisely resolve the time (load) history of tested samples. Further, relaxation is to be avoided (originating either from the material due to its time-dependent behavior or testing device). Synchrotron facilities allow these limits to be broken with tens of Hertz scan acquisition rate, using classical methods [25]. Exceptional experimental set-ups are required in addition to very bright X-ray beams.

The present study aims at demonstrating that using the recently introduced projection-based DVC technique (*i.e.*, P-DVC [23,35,17,19]) allows fast mechanical tests to be performed *in situ* and monitored in a lab CT-scanner even with non trivial kinematics. In the present case, a Wedge Splitting Test [37,6] is performed on a castable refractory *in less than one minute*. Last, after discussing the sensitivity on the measured crack tip position, the fracture toughness is estimated.

In Section 2, the principle of projection-based DVC is recalled. The analyzed wedge splitting test is presented in Section 3. Section 4 is devoted to the numerical simulations of the test via extended finite element (X-FEM) analyses from which a reduced kinematic basis is constructed for the P-DVC procedure. With the latter, the wedge splitting test is studied and results are reported in Section 5. In particular, the sensitivity of the P-DVC results to the crack length is investigated, and a confidence interval on the fracture toughness is obtained.

## 2 Projection-based Digital Volume Correlation

This section aims at recalling the basics of DVC and P-DVC, together with the notations used herein.

First, a flat field (*i.e.*, image of the X-ray source on the detector with no imaged sample) $I_0(\boldsymbol{r})$ is acquired. Then, the sample is positioned between the source and the detector on a rotation stage, whose angular direction is parallel to the detector columns. For many angles $\theta$ spanning $[0, 2\pi]$, images are acquired $I(\boldsymbol{r}, \theta)$. From this series of images, *projections* are computed as

$$p(\boldsymbol{r}, \theta) = \log(I_0(\boldsymbol{r})/I(\boldsymbol{r}, \theta)) \tag{1}$$

The 3D volume, $f(\boldsymbol{x})$, is such that its projection (*i.e.*, sum of absorption coefficient along each point $\boldsymbol{x}$ of the beam ray hitting the detector at position $\boldsymbol{r}$) should match the recorded projection $p(\boldsymbol{r}, \theta)$. This property is a linear relationship between $f$ and $p$

$$\mathit{\Pi}_\theta[f(\boldsymbol{x})] = p(\boldsymbol{r}, \theta) \tag{2}$$

It is the inversion of this linear system for a large set of angles $\theta$ that is called the *reconstruction*. Many algebraic reconstruction algorithms are based on the minimization of the quadratic difference of the above left and right members [20]

$$f(\boldsymbol{x}) = \mathrm{Argmin}_{\varphi(\boldsymbol{x})} \sum_{\boldsymbol{r},\theta} \left(\mathit{\Pi}_\theta[\varphi(\boldsymbol{x})] - p(\boldsymbol{r}, \theta)\right)^2 \tag{3}$$

Beam-hardening, which is the consequence of the X-ray source not being monochromatic, may have to be corrected on $p$ prior to the reconstruction step so that Equation (2) is obeyed as closely as possible [15].

When following the 3D kinematics of a medium, a classical procedure is to reconstruct a series of such tomographic images, $f(\boldsymbol{x},t)$ [7]. The displacement field, $\boldsymbol{u}(\boldsymbol{x},t)$, is estimated using DVC [4,5,39,31], which is based on the assumption of the conservation of the coefficient of absorption (or "gray level" of the reconstructed volume). Introducing the Eulerian displacement field, it follows that

$$f(\boldsymbol{x},t) = f(\boldsymbol{x}-\boldsymbol{u}(\boldsymbol{x},t), t=0) \tag{4}$$

where the time parameter, $t$, is used here merely to label the different states where a tomographic image is captured. It may thus be used as a superscript. Hence $f^0(\boldsymbol{x})$ designates the reference volume and $p^0(\boldsymbol{r},\theta)$ its projections.

To solve the above (inverse) problem, the displacement field is discretized in space. When using global DVC [31], it is often chosen to use a finite-element mesh fitted to the sample geometry, as it provides a natural interface with numerical simulations [30,16,9]. Thus the displacement field is written as

$$\boldsymbol{u}^t(\boldsymbol{x}) = \sum_i u_i^t \boldsymbol{\psi}_i(\boldsymbol{x}) \tag{5}$$

where $\boldsymbol{\psi}_i$ are finite element shape functions, and $u_i^t$ the corresponding nodal displacements, which are gathered in the column vector $\{\boldsymbol{u}^t\}$. A variational formulation is usually chosen, so that $\{\boldsymbol{u}^t\}$ is obtained from the minimization of the quadratic differences

$$\{\boldsymbol{u}^t\} = \mathrm{Argmin}_{\{\boldsymbol{v}\}} \sum_{\boldsymbol{x}} \Big( f^0(\boldsymbol{x}-v_j\boldsymbol{\psi}_j(\boldsymbol{x})) - f^t(\boldsymbol{x}) \Big)^2 \tag{6}$$

The recently introduced variant of DVC, namely, projection-based DVC (or P-DVC [23,35,18,17,19]) exploits a similar principle but on the projections. Hence the minimization problem is rewritten as

$$\{\boldsymbol{u}^t\} = \mathrm{Argmin}_{\{\boldsymbol{v}\}} \sum_{\boldsymbol{r},\theta} \Big( \mathit{\Pi}_\theta[f^0(\boldsymbol{x}-v_j\boldsymbol{\psi}_j(\boldsymbol{x}))] - p^t(\boldsymbol{r},\theta) \Big)^2 \tag{7}$$

or, in order to minimize the effect of systematic bias of the detector, one may exploit the fact that the undeformed projection is already known

$$u_i^t = \mathrm{Argmin}_{v_j} \sum_{\boldsymbol{r},\theta} \Big( \mathit{\Pi}_\theta[f^0(\boldsymbol{x}-v_j\boldsymbol{\psi}_j(\boldsymbol{x})) - f^0(\boldsymbol{x})] - (p^t(\boldsymbol{r},\theta) - p^0(\boldsymbol{r},\theta)) \Big)^2 \tag{8}$$

Although the two formulations look quite similar, P-DVC now offers new opportunities. It is worth noting that the microstructure of the sample is known as soon as $f^0$ has been computed. The remaining unknowns are the displacement components $u_i^t$, which are sparser than $f^t$ itself (*i.e.*, the kinematic degrees of freedom are much fewer than the number of voxels). Hence, there is no need for using as many projections to track the motions as when one wishes to evaluate the 3D image of the deformed microstructure. Several orders of magnitudes savings can be reached [23].

Moreover, using a time discretization that is nonlocal

$$\boldsymbol{u}(\boldsymbol{x},t) = \sum_{i,j} u_{ij}\boldsymbol{\psi}_i(\boldsymbol{x})\phi_j(t) \tag{9}$$

where $\phi_j$ are chosen time functions, allows the regularity of the temporal changes to be set very early on in the formulation. It restores the status of $t$ as a real time parameter in the sense that rotation $\theta(t)$, but also mechanical loading, vary continuously with $t$. With such a formulation, only one projection per load level is needed with the natural benefit of carrying out an uninterrupted mechanical test where projections are now captured on the fly [18].

The variational formulation is a mere extension of the previous one. For the sake of notation conciseness, the projection differences are denoted as

$$\rho(\boldsymbol{r},t) = p^t(\boldsymbol{r},\theta(t)) - p^0(\boldsymbol{r},\theta(t)) \tag{10}$$

and

$$\{\boldsymbol{u}\} = \mathrm{Argmin}_{\{\boldsymbol{v}\}} \sum_{\boldsymbol{r},t} \Big( \Pi_{\theta(t)}[f^0(\boldsymbol{x} - v_{kl}\boldsymbol{\psi}_k(\boldsymbol{x})\phi_l(t)) - f^0(\boldsymbol{x})] - \rho(\boldsymbol{r},t) \Big)^2 \tag{11}$$

where $\{\boldsymbol{u}\}$ gathers all unknown amplitudes $u_{ij}$. The above minimization is performed by a Gauss-Newton algorithm as for standard DVC [9].

Although none were implemented in the present study, additional features may be implemented to further simplify processing and enhance both result quality and convergence speed:

- The separated form of Equation (9) motivates a further reduction in the number of unknowns as performed in Proper Orthogonal Decomposition (POD) and Proper Generalized Decomposition (PGD) analyses [10,28,21,22]. The driving idea is to search for "modes," labeled by an index $k$, composed of a spatial part $\widetilde{\boldsymbol{\psi}}^k(\boldsymbol{x}) = a_i^k\boldsymbol{\psi}_i(\boldsymbol{x})$ and a temporal part, $\widetilde{\phi}^k(t) = b_j^k\phi_j(t)$, and, if both of these fields are normalized to 1, an amplitude $c^k$ such that

$$\boldsymbol{u}(\boldsymbol{x},t) = \sum_k c^k\widetilde{\boldsymbol{\psi}}^k(\boldsymbol{x})\widetilde{\phi}^k(t) \tag{12}$$

  A greedy approach [11], which is based on the determination of one mode at a time, is an efficient way of handling this problem, which then reduces to the determination of *the* additional mode $\widetilde{\boldsymbol{\psi}}^k$ and $\widetilde{\phi}^k(t)$ that will account for most of the "residual difference," *i.e.*, the field $\rho$ from which all contributions of previous modes $1, ..., k-1$ have been subtracted. This PGD-type strategy proved to be extremely efficient in the context of P-DVC [18].
- Use a substitute to time. For instance, a mechanical test may provide a load signal $F(t)$ that may be more legitimate than time to design a temporal basis, and hence $\phi_j(t) = \hat{\phi}_j(F(t))$ may be better suited than regular functions of time. Additionally, an improper geometry calibration may suggest that $\theta(t)$ may be used with sine and cosine contributions as other temporal basis functions, $\phi_j(t) = \sin(\theta(t))$ or $\phi_j(t) = \cos(\theta(t))$. Since those basis functions are unconstrained, the present flexibility is a powerful way to include prior knowledge or expectations into the problem formulation.

– Another efficient approach is to rely on the guidance of a mechanical model. The latter can be used to extract candidate fields either in space or time and both that are firmly founded from a prior mechanical knowledge [16,9]. Sensitivity fields — *i.e.*, differential displacement fields resulting from the variation of a parameter from the mechanical modeling (be it from constitutive properties, boundary conditions, or sample geometry) — are emblematic of such examples [36].

This list does not provide a unique pathway to the solution. However, if offers a wealth of opportunities to exert one's expertise, knowledge or intuition. The more suited the latter to the case of interest, the higher the reward. It may be feared that too strong a guidance may be provided to the analysis. However, let us stress that residuals will never be "explained" by an inappropriate model, and hence the level of residuals (or its likelihood) may then be used to falsify the model and possibly correct it [27]. A possibly wrong model may not be detected (for instance an elastoplastic medium that is tested only within its elastic domain cannot prove the inadequacy of a purely elastic model) but this is the fate of any scientific statement according to Popper [29]. One can only assess the consistency of a model with a given set of observations, which does not prove that the model be valid. All models are wrong, those considered valid are simply awaiting for their falsification.

## 3 Wedge Splitting Test

The considered material is a castable refractory. It is composed of an alumina matrix with mullite-zirconia aggregates whose granulometry is in the millimeter range (*i.e.*, the maximum aggregate size is 3 mm). The sample was fired at 1400°C for 5 h. Numerous pores were trapped within the sample before setting. This microstructure produces a large contrast in X-ray absorption, and hence 3D images display a very clear contrast, which is beneficial for DVC purposes [3,9]. The sample was first cast in a cylindrical mould (60 mm in height (*i.e.*, $z$-direction), and 72 mm in diameter). Then, a 4-mm wide notch was ground using the lateral grooves that were present in the as-cast geometry. The latter was designed for easy initiation of the crack from the notch, but also to guide the cracked surface during stable propagation. To this aim, a chevron-shape was chosen so that the crack front length increased as the crack propagated. The apex of the V is located 13.5 mm from the top surface. Figure 1 illustrates the geometry from three orthogonal sections about the specimen center (*i.e.*, the three median planes).

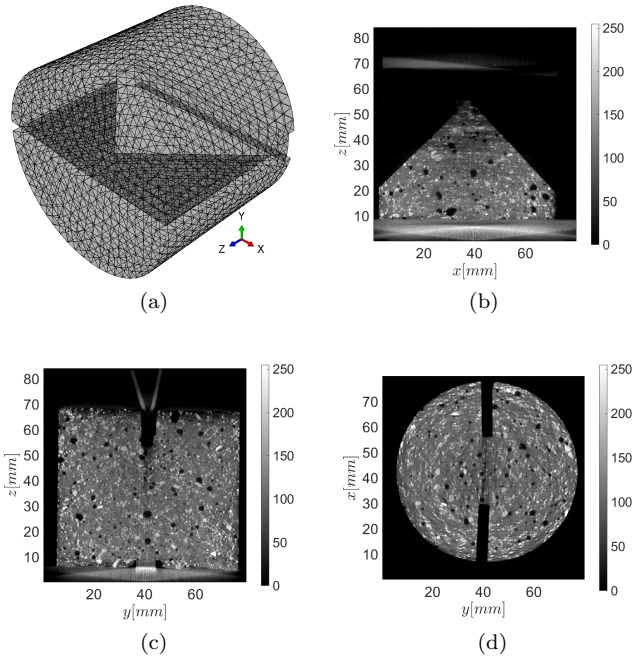


Fig. 1: Sample geometry (a) and mid-sections along (b) $(x, z)$ plane, (c) $(y, z)$ plane, and (d) $(x, y)$ plane.

A 30° wedge made of wood was stiffened with an aluminum alloy plate bent to the wedge angle to prevent too strong surface damage. This wedge was forced down into the notch in order to open a mode I crack that propagated in the mid-$y$ plane, as can be seen at the top of Figure 1(b). The crack front, which was parallel to the $x$ axis, had thus an increasing length as it propagated down through the sample, thereby providing the sought enhanced stability.

Before starting the experiment, the sample was first carefully scanned. The X-ray tube (W target) was set to 210 kV, with a current of 150 µA. A 0.5 mm thick copper plate was used to limit beam hardening. The reconstruction was computed with 1,200 projections over one full revolution (*i.e.*, 360° range). Each projection was acquired with an average over 30 frames (*i.e.*, 3 s per projection) to reduce noise. Including the sample rotation time, the overall acquisition time was 84 min. Because of the coarse microstructure and specimen size, the resolution was set to 248 µm per voxel for 342×486 pixel projections. The same scanning protocol was used at the end of the fracture experiment in order to allow for the validation of the entire analysis, and have access to the fracture surface geometry.

Because the P-DVC algorithm exploits the connection between projections and the reconstructed volume, it is important that this correspondence be trustful. In particular, beam hardening (BH) artifacts should be reduced as much as possible. Beam hardening results from the high absorption of low energy X-rays that affects the energy spectrum of the beam as it traverses the medium, and hence introduces an artificial contrast especially close to external surfaces. A large part of BH can

be eliminated through a nonlinear correction of the gray levels in the projections (thus as a preprocessing step) [15]. This correction was first calibrated from the reconstruction, and then the same systematic transformation was performed on each projection. In the present case, a cubic polynomial revealed sufficient to account for most of the BH artifacts.

It is also noteworthy that the reconstruction itself may not be strictly identical to solving Equation (3). In particular, Fourier-based methods, such as the so-called Feldkamp algorithm [13] for cone-beam reconstruction, involve an inherently distinct discretization scheme for voxels as that involved in a mere projection algorithm. In contrast, algebraic reconstruction methods such as SIRT [20] are based on the direct solution to Equation (3), using precisely the same projection operator as that used in P-DVC. Hence, it is beneficial to use SIRT-like procedures for reconstructions. However, such approaches are also less computationally efficient than Fourier-based methods. Thus, the choice was made to first perform a Feldkamp reconstruction and then run on the obtained volume a few (typically ten) SIRT iterations to have a consistent solution. Projections and reconstructions are performed with the ASTRA toolbox [38] and geometrical parameters given by the tomograph calibration. To evaluate the quality of the reconstruction, one can consider the projection residuals, namely, the difference between the measured projection $p(\boldsymbol{r}, \theta)$ and the projection of the reconstructed volume $\mathit{\Pi}_\theta[f(\boldsymbol{x})]$.

Figure 2 shows such a residual field when the projection direction lies along the $x$-axis (*i.e.*, parallel to the notch plane), which is the most sensitive to the very precise reconstruction of the notch edge. The latter is faintly marked in this residual field, but the gray level difference is comparable to the more massive, red, rectangular shaped part in the lower part that is due to a systematic difference of sensitivity of the four-quadrant detector. It means that instrumental acquisition artifacts become the limiting factor in the reconstruction (more than noise). In quantitative terms, the root mean square (RMS) residual per pixel is 0.153 arbitrary units as compared to a full dynamic range of the projection of about 8 (same) arbitrary units. This residual requires an appropriate beam hardening correction to reach such remarkably low levels.

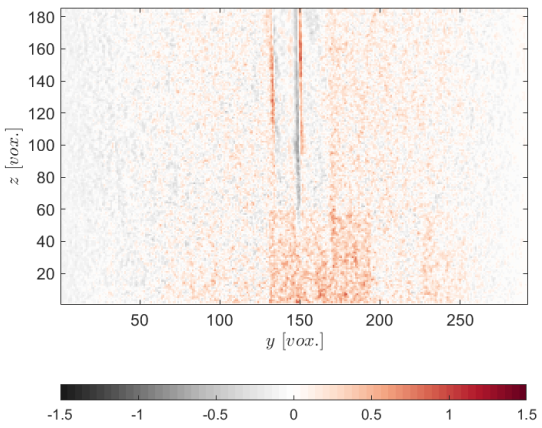


Fig. 2: Projection residuals for an orientation perpendicular to the $x$-axis (similar to that of Figure 1(b)).

The wedge splitting test was conducted *in situ*. A testing machine specially designed for the CT scanner was used to apply the load on the wedge [9]. The maximum applied load was close to 6 kN (well below the machine capacity of 20 kN). Figure 3(a) shows the force-displacement curve that was recorded during the entire experiment, which lasted 36 s. Such a short duration is to be compared to the time devoted to acquiring the reference volume (*i.e.*, close to 1h30 or 5,400 s).

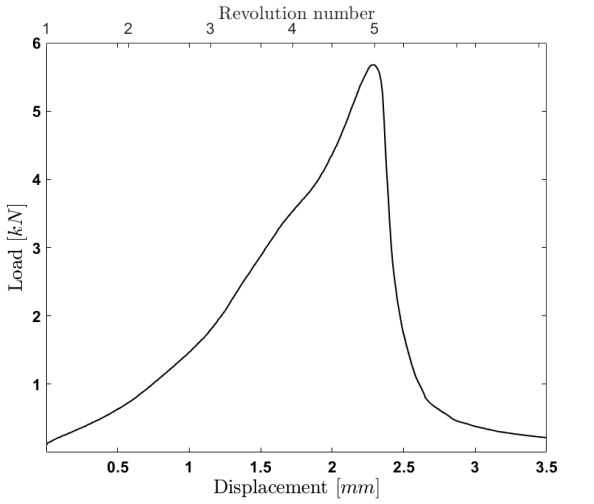


(a)

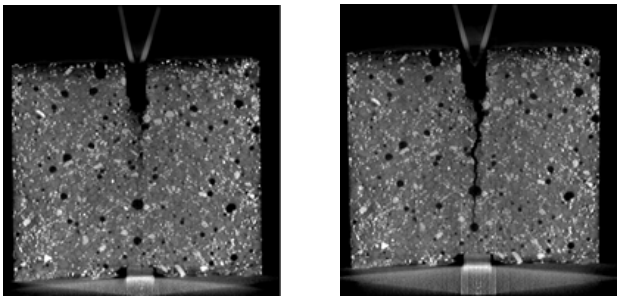

(b) (c)

Fig. 3: (a) Load-displacement curve of the wedge splitting test. Note that prior to recording the curve, a full revolution was acquired in the low acquisition mode with no applied load. The rotation number is shown in the graduation of the top axis. (b) $(y, z)$ mid-plane section through the sample in its initial state, (c) same $(y, z)$ section at the end of the test.

All along the loading history (up to peak force), and while the rotation was taking place (both loading and rotation were simultaneously and continuously activated), radiographs were acquired at a fast rate. The X-ray source was held at similar conditions to those used for initial and final tomography acquisitions (*i.e.*, 210 kV, 150 µA current, copper plate), and the resolution was also unchanged (*i.e.*, 1 voxel $\equiv$ 248 µm). The rate of acquisition was 10 fps, similar to that of the reference tomographic images. However, instead of averaging over 30 frames, single frames were recorded (giving rise to a much higher level of noise, but allowing for a higher rotation rate with no motion blur). During the first revolution, no loading was applied (the wedge was simply positioned in contact with the sample top notch, with minimal static load). This first stage was performed to ensure

that the P-DVC algorithm could be run on the same data quality as the actual mechanical test, and the absence of measured strain constitutes a validation of the approach in real conditions. The previously reported projection residual levels and the illustration in Figure 2 were obtained.

During the 36 s duration of the test, a 1,700° range was covered (or, in other words, 4.72 full revolutions including the first revolution without load). The sample deformation and the penetration of the wedge by about 3 mm are such that classical reconstructions could not be performed based on this set of 425 radiographs. However, as earlier mentioned, the motivation is to utilize P-DVC for the analysis of the detailed (and load-resolved) kinematics all along the test.

## 4 FE Model

The reference volume is used to tailor a tetrahedral mesh to the exact sample geometry. As shown in Figure 4, the mesh is composed of 5,201 nodes, and 25,767 4-noded tetrahedral elements. Because of its fine microstructure, the material is modeled as homogeneous. Moreover, its behavior is considered as elastic, with parameter values $E = 58$ GPa and $\nu = 0.1$ issued from prior tests.

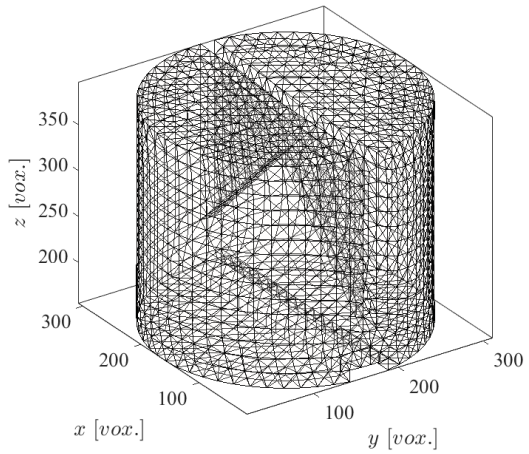


Fig. 4: Mesh used to simulate the experiment with Abaqus. Only surface elements are shown for a better readability. The same mesh, which was designed to fit precisely the 3D image, is used for P-DVC.

To model fracture, an extended finite element (X-FEM) strategy (as implemented in Abaqus [1]) is used. In the following, no crack propagation will be modeled. Rather, several crack lengths will be considered to analyze different stages. Consequently, the sample geometry at any stage is fully described by the mesh, and a single extra parameter $h$ that quantifies the advance of the crack front over

the mid $y$ plane from the initial geometry where conventionally $h = 0$. However, it is worth noting that the X-FEM framework allows for modeling such a propagation, ruled either by a critical stress intensity factor or by a more sophisticated description such as a cohesive zone model, whose finality is to enrich the linear elastic fracture propagation model. Thus the limiting factor is not modeling but rather the experimental sensitivity to additional parameters.

Let us emphasize that the very same mesh is used to perform all P-DVC analyses. P-DVC may theoretically be performed using all degrees of freedom allowed by the mesh (*i.e.*, 15,603 DOFs). However, this would be vain since the sensitivity to each individual kinematic DOF is low and would result in a very noisy displacement field. Thus, rather than considering a totally unconstrained kinematics, it is rewarding to exploit the prior knowledge about the mechanical behavior, which is essentially a linear problem when the crack front does not propagate. Yet, a number of unknowns accounting for the boundary conditions remains to be determined. These unknowns are collectively called $\{\boldsymbol{p}\} = \{p_i\}$, for $i = 1, ..., N_p$. Concerning time, when the first rotation is considered, because no load is applied, a single time function (*i.e.*, a constant equal to unity) is chosen. For the four following rotations where the wedge penetration increases at a constant velocity, two time functions were selected in the form of a constant and a linear evolution. Notwithstanding this global evolution spanning the entire loading period, restricted time windows could be chosen to speed up the computation time.

In order to add the time dimension to the problem, with the above temporal shape functions, $\phi_j(t)$, additional unknowns, $p_{ij}$, are introduced such that $p_i(t) = p_{ij}\phi_j(t)$. To ease notations, one may introduce a multi-index notation $\boldsymbol{i} = (i_1, i_2)$, and hence $p_{i_1\ i_2}$ may be denoted as $p_{\boldsymbol{i}}$. Note that the same convention may also hold for the nodal displacement $i_1$ along the temporal basis function $\phi_{i_2}$, $u_{i_1\ i_2} = u_{\boldsymbol{i}}$.

To account for the boundary conditions, one may note that the top surface is partitioned in two because of the notch, and the wedge prescribes different kinematics on both sides. Ideally, only the motion along the contact line should matter, and all other surfaces but the base should be free. However, because of possible nonlinearities taking place along this contact line, it is considered safer to introduce as unknown the mean rigid body motions (6 DOFs) of the two top surfaces (*i.e.*, 12 unknowns). This may not be completely faithful to reality, as it neglects the possible deformation of these top surfaces. Yet, to account for the bulk kinematics, and especially for crack advance, the discarded modes are assumed to have a negligible influence. In addition, the bottom surface is also treated as rigid giving rise to six more DOFs, or a total of 18 DOFs. Such parameterization works, yet a significant projection residual remains in the lower part of the sample after the P-DVC analysis, thereby signaling that this kinematics is not fully satisfactory. A closer examination of the bottom boundary condition shows that the sample is essentially resting on a thin groove machined on the sample opposite to the opening wedge in order to prevent its rotation. As a result, a flexure of the bottom surface is likely to happen. This effect is introduced through an extra DOF in the form of an angular discontinuity (rotation about the axis parallel to $x$ in the bottom plane). With these 19 spatial DOFs, a very significant decrease in the projection residuals occurred, and hence, all the following analyses were performed with these 19 spatial DOFs, which — when dressed with the two temporal shape functions — amount to a total of 38 DOFs.

For any set of parameters $\{\boldsymbol{p}\}$, the FE model provides the sensitivity coefficients $S_{ij} = \partial u_i / \partial p_j$ of nodal displacement $i$ with respect to boundary condition DOF $j$. Let us note that the problem is linear elastic, and hence the sensitivities are constant. The only possible nonlinearity would come from crack propagation. To facilitate the solution to this problem, crack propagation during one revolution was neglected. However, different crack lengths $h$ were considered in parallel as independent problems, and the one giving rise to the smallest residual was selected.

## 5 Results

As earlier discussed, the first revolution was performed with virtually no load. The evaluation of the residuals leads to an RMS estimate of 0.15 arbitrary unit showing that the algorithm was successful in achieving a very low value (*i.e.*, about 2 % of the dynamic range). To complement this validation, one may check that the measured kinematics is essentially that of a rigid body. The von Mises equivalent strain was determined in the volume from the measured displacement field, giving a volume average of $4 \times 10^{-3}$. This also provides an estimate of the displacement uncertainty by computing the RMS value of the nodal displacements after having removed the rigid body motion. For all components, this uncertainty is of order 0.01 voxel.

Figure 5 shows the 3D displacement field measured for the fifth revolution, along the mid-$x$ cross-section. Although the most salient feature is the crack opening in Mode I (along $y$), which amounts to about 2 voxels, or 500 µm, it is more clearly observed in Figure 6 that some mode II and III components also appear as a result of a possibly irregular slip of the wedge as it penetrates into the notch.

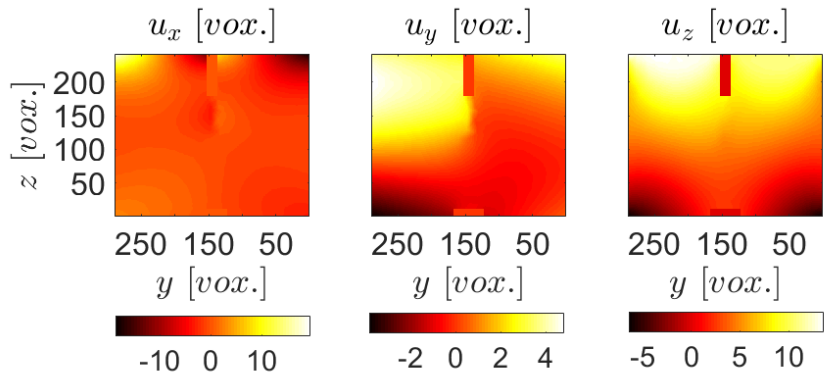


Fig. 5: Three components of the displacement field along the mid-$x$ plane at the fifth and last revolution. All values are expressed in voxels (1 voxel $\equiv$ 248 µm)).

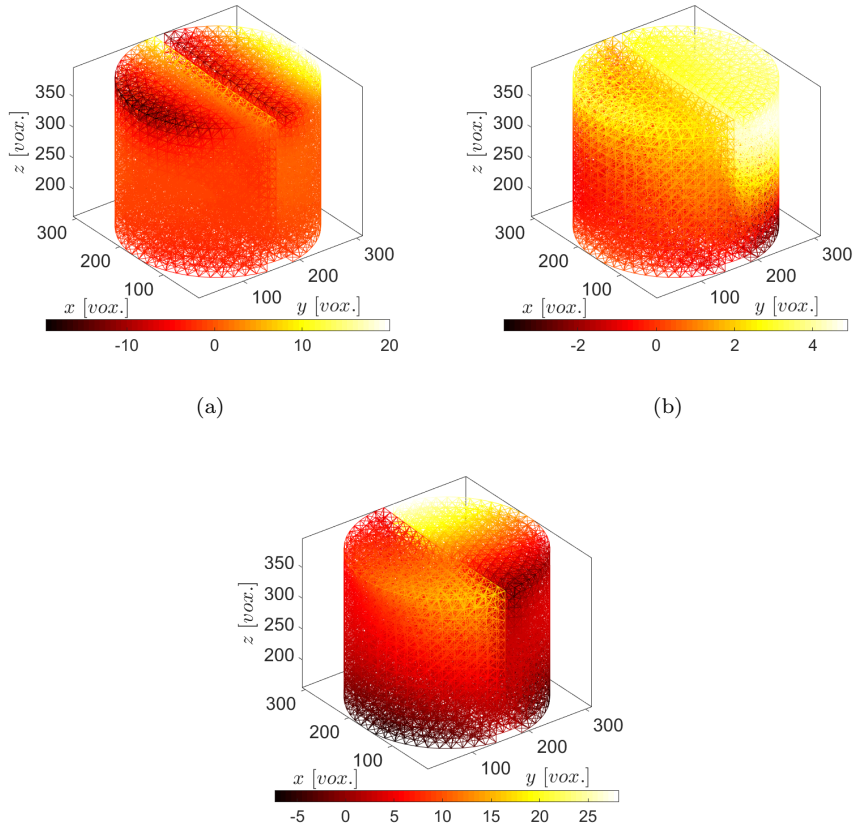


Fig. 6: 3D rendering of the deformed medium. (a) $u_x$, (b) $u_y$, (c) $u_z$ components expressed in voxels (1 voxel $\equiv$ 248 µm)). The displacement discontinuity shows that a significant mode III (a) and mode II (c) are present, although mode I is dominant (b).

Figure 7 shows the corresponding projection residual before and after registration for an orientation of the sample that is such that the projection direction is essentially along $x$. This orientation is the most sensitive to the crack opening fields. The RMS value of the residual is 0.29 arbitrary unit, a much higher level than that obtained with the first revolution (no load), yet quite small as compared to the dynamic range of projections, which is about 8 arbitrary units.

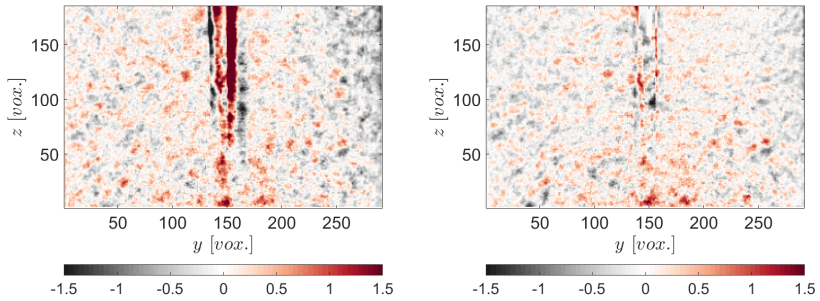


Fig. 7: Residuals at the fifth and last revolution for a crack length equal to half its maximum size (which is observed to minimize the residual). The color bar is graded in arbitrary units, and should be compared to the dynamic range of projections, which is about 8 (arbitrary units. (a) before registration, (b) after registration. The registration brings the RMS residual from 0.46 down to 0.29 arbitrary unit.

In the previous figures, the crack front position is chosen to be at mid height from its initial position to the bottom surface, *i.e.*, $h = h_{\max}/2$ where the minimum value of the residual is reached. However, the minimum is shallow and rather suggests that the crack tip position lies in between $h_{\max}/2$ and $h_{\max}$.

Let us comment some more on the accuracy of the determination of the crack front position. It is to be noted that the latter is mostly insensitive for all angular orientations not parallel to the $x$-axis. To evaluate the sensitivity to the crack front position, one may consider the difference in residuals along the $x$ projection direction for the two probed $h$ positions (*i.e.*, $h = h_{\max}/2$ and $h = h_{\max}$). This difference is essentially the increment of displacements $\delta\boldsymbol{u}$ due to the crack front advance, contracted with the image gradient $\boldsymbol{\nabla} f$ and projected $\Pi_\theta[\delta\boldsymbol{u} \cdot \boldsymbol{\nabla} f]$. This field is the one to be used when evaluating the crack front position, through the evaluation of having lower or higher residuals when this field is added to the present residual values. Figure 8 shows such sensitivity field. It is observed that most of the signal is concentrated along the notch faces (because of the large contrast) and away from the crack because of the larger displacement expected there due to a lever effect. Although this sensitivity displays significant features, its amplitude is about the level of uncertainty, and hence, it is unfortunately vain to have a finer determination of the crack front position with the present data.

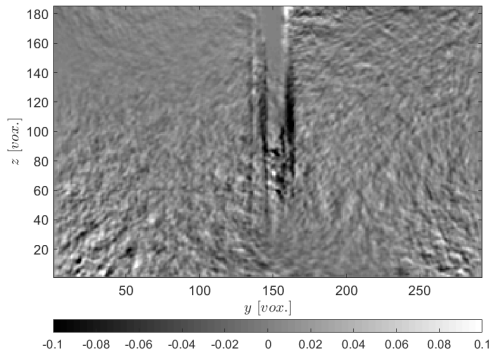


Fig. 8: Projection residual difference (for a projection direction along $x$) obtained for two proposed crack front positions $h = h_{\max}/2$ and $h = h_{\max}$.

Last, it is proposed to evaluate bounds for the toughness (*i.e.*, critical stress intensity factor) from the two limiting values $h_{\max}/2$ and $h_{\max}$ of the crack front. The stress intensity factor $K_I$ was evaluated with the standard procedures of Abaqus [1] at different points along the crack front for the two proposed crack lengths. (Note that because of the V shape of the notch, the crack front length is shorter when $h = h_{\max}/2$, and thus $y$ spans a smaller interval, than when $h = h_{\max}$ where the entire sample width is concerned.) The fluctuations of $K_I$ along the front are not meaningful, but the mean values 3.9 MPa$\sqrt{\text{m}}$ and 2.2 MPa$\sqrt{\text{m}}$ for the two extreme crack front positions provide bounds for the toughness $K_c$. Consequently, a first order estimate of $K_c$ is $3 \pm 0.8$ MPa$\sqrt{\text{m}}$. It is noteworthy that the Young's modulus was not evaluated in the present experiment (*i.e.*, no load data were considered). Rather its value was taken from an independent estimate ($E = 58$ GPa). Hence, the present experiment should only claim for the evaluation of $K_c/E$, a combination which is a kinematic quantity (*i.e.*, $0.05 \pm 0.015$ $\sqrt{\mu\text{m}}$).

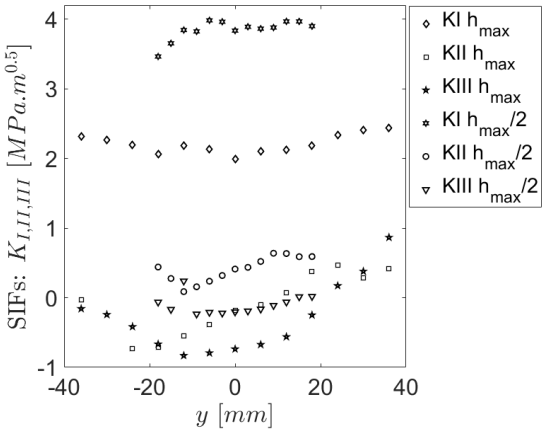


Fig. 9: Mode I, II and III stress intensity factors evaluated along the crack front for $h = h_{\max}/2$ ($\star$, $\circ$ and $\triangledown$) and $h = h_{\max}$ ($\diamond$, *square* and $\star$).

It was earlier noted that modes II and III were present in this experiment. From the FE model, the corresponding stress intensity factors for these modes and the two possible scenarios for the crack front position are straightforwardly accessible. They are shown in Figure 9. For both scenarios, their level remains less than 1 MPa.m$^{1/2}$. Although these values are smaller than the corresponding mode I data, they suggest to consider with caution the above toughness evaluation.

## 6 Conclusions

Projection-based Digital Volume Correlation (P-DVC) was reviewed and applied to a fracture test performed in situ in a lab CT-scanner, which challenges the methodology for an extremely fast (*i.e.*, sub-minute) test as compared to common practice (*i.e.*, one high quality scan would take up to 5,400 s in the present case). It has been shown that in spite of the degraded quality of projections due to fast acquisition, noise was still not a limiting factor (as compared to detector imperfections). The P-DVC algorithm could resolve the kinematics of the test and provide an estimate of the crack front advance. A confidence interval on the toughness of the studied refractory was finally obtained. Thus, a complete analysis of the test kinematics was achieved.

The kinematic degrees of freedom were here selected in order to achieve a good (although not perfect) description of the kinematics through 19 different fields. A more systematic determination of the appropriate basis would be highly desirable. Although a very efficient screening can be provided by model reduction techniques [18,19], once a first kinematic basis is chosen, this initial selection of a sufficient large kinematic space to embed the solution is computationally very

demanding. This point is a direction of progress that would be very beneficial to the present method.

**Acknowledgements** This work benefited from the support of the French "Agence Nationale de la Recherche" through the "Investissements d'avenir" program under the reference "ANR-10-EQPX-37 MATMECA." The PhD project of RV is supported through grant #2018/23081-0, São Paulo Research Foundation (FAPESP). The authors thank Profs. R.B. Canto and J.A. Rodrigues for fruitful discussions.

## Competing interests

The authors declare no competing interests.

## References

1. GUI Abaqus. Abaqus 6.11, 2011.
2. J Baruchel, J Y Buffière, E Maire, P Merle, and G Peix, editors. *X-Ray Tomography in Material Sciences*. Hermès Science, Paris (France), 2000.
3. B K Bay. Methods and applications of digital volume correlation. *J. Strain Analysis*, 43:745–760, 2008.
4. B K Bay, T S Smith, D P Fyhrie, and M Saad. Digital volume correlation: three-dimensional strain mapping using X-ray tomography. *Exp. Mech.*, 39:217–226, 1999.
5. M Bornert, J M Chaix, P Doumalin, J C Dupré, T Fournel, D Jeulin, E Maire, M Moreaud, and H Moulinec. Mesure tridimensionnelle de champs cinématiques par imagerie volumique pour l'analyse des matériaux et des structures. *Inst. Mes. Métrol.*, 4:43–88, 2004.
6. E Brühwiler and FH Wittmann. The wedge splitting test, a new method of performing stable fracture mechanics tests. *Eng. Fract. Mech.*, 35(1):117–125, 1990.
7. J Y Buffière, E Maire, J Adrien, J P Masse, and E Boller. In Situ Experiments with X ray Tomography: an Attractive Tool for Experimental Mechanics. *Exp. Mech.*, 50(3):289–305, 2010.
8. J Y Buffière, E Maire, P Cloetens, G Lormand, and R Fougères. Characterisation of internal damage in a MMCp using X-ray synchrotron phase contrast microtomography. *Acta Mater.*, 47(5):1613–1625, 1999.
9. A Buljac, C Jailin, A Mendoza, T Taillandier-Thomas, A Bouterf, J Neggers, B Smaniotto, F Hild, and S Roux. Digital Volume Correlation: Review on Achievements and Challenges. *Exp. Mech.*, 58(5):661–708, 2018.
10. F Chinesta, A Ammar, and E Cueto. Recent advances and new challenges in the use of the proper generalized decomposition for solving multidimensional models. *Arch. Comput. Meth. Eng.*, 17(4):327–350, 2010.
11. T H Cormen. *Introduction to algorithms*. MIT press, 3rd edition, 2009.
12. J Desrues, G Viggiani, and P Bésuelle, editors. *Advances in X-ray Tomography for Geomaterials*. Wiley / ISTE, London (UK), 2006.
13. L A Feldkamp, L C Davis, and J W Kress. Practical cone beam algorithm. *J. Opt. Soc. Am.*, A1:612–619, 1984.
14. A Guvenilir, T M Breunig, J H Kinney, and S R Stock. Direct observation of crack opening as a function of applied load in the interior of a notched tensile sample of Al-Li 2090. *Acta Mater.*, 45(5):1977–1987, 1997.
15. Gabor T Herman. Correction for beam hardening in computed tomography. *Physics in Medicine & Biology*, 24(1):81, 1979.
16. F Hild, A Bouterf, L Chamoin, F Mathieu, J Neggers, F Pled, Z Tomičević, and S Roux. Toward 4D Mechanical Correlation. *Adv. Mech. Simul. Eng. Sci.*, 3(1):1–26, 2016.
17. C Jailin, A Bouterf, M Poncelet, and S Roux. In situ $\mu$ct-scan mechanical tests: Fast 4d mechanical identification. *Experimental Mechanics*, 57(8):1327–1340, 2017.
18. C Jailin, A Buljac, A Bouterf, F Hild, and S Roux. Fast four-dimensional tensile test monitored via X-ray computed tomography: Single projection based Digital Volume Correlation dedicated to slender samples. *The Journal of Strain Analysis for Engineering Design*, 53(7):473–484, 2018.

19. C Jailin, A Buljac, A Bouterf, F Hild, and S Roux. Fast four-dimensional tensile test monitored via x-ray computed tomography: Elastoplastic identification from radiographs. *The Journal of Strain Analysis for Engineering Design*, 54(1):44–53, 2019.
20. A C Kak and M Slaney. *Principles of Computerized Tomographic Imaging*. Society of Industrial and Applied Mathematics, Society of Industrial and Applied Mathematics, 2001.
21. P Ladevèze. *Nonlinear computational structural mechanics: new approaches and non-incremental methods of calculation*. Springer Science & Business Media, 2012.
22. P Ladevèze. PGD in linear and nonlinear computational solid mechanics. In *Separated Representations and PGD-Based Model Reduction*, pages 91–152. Springer, 2014.
23. H Leclerc, S Roux, and F Hild. Projection Savings in CT-based Digital Volume Correlation. *Exp. Mech.*, 55(1):275–287, 2015.
24. E Maire, J Y Buffière, L Salvo, J J Blandin, W Ludwig, and J M Létang. On the application of X-ray microtomography in the field of materials science. *Adv. Eng. Mat.*, 3(8):539–546, 2001.
25. E Maire, C Le Bourlot, J Adrien, A Mortensen, and R Mokso. 20-Hz X-ray tomography during an in situ tensile test. *Int. J. Fract.*, 200(1):3–12, 2016.
26. E Maire and P J Withers. Quantitative X-ray tomography. *Int. Mat. Rev.*, 59(1):1–43, 2014.
27. J Neggers, F Mathieu, F Hild, S Roux, and N Swiergiel. Improving full-field identification using progressive model enrichments. *International Journal of Solids and Structures*, 118:213–223, 2017.
28. A Nouy. A priori model reduction through proper generalized decomposition for solving time-dependent partial differential equations. *Comput. Meth. Appl. Mech. Eng.*, 199(23):1603–1626, 2010.
29. Karl R Popper. *Logik der Forschung*. Verlag von Julius Springer, Vienna (Austria), 1935.
30. J Rannou, N Limodin, J Réthoré, A Gravouil, W Ludwig, M C Ba\"\ietto, J Y Buffière, A Combescure, F Hild, and S Roux. Three dimensional experimental and numerical multiscale analysis of a fatigue crack. *Comp. Meth. Appl. Mech. Eng.*, 199:1307–1325, 2010.
31. S Roux, F Hild, P Viot, and D Bernard. Three dimensional image correlation from X-Ray computed tomography of solid foam. *Comp. Part A*, 39(8):1253–1265, 2008.
32. L Salvo, P Cloetens, E Maire, S Zabler, J J Blandin, J Y Buffiere, W Ludwig, E Boller, D Bellet, and C Josserond. X-ray micro-tomography an attractive characterisation technique in materials science. *Nucl. Instr. Meth. Phys. Res. B*, 200:273–286, 2003.
33. T S Smith, B K Bay, and M M Rashid. Digital volume correlation including rotational degrees of freedom during minimization. *Exp. Mech.*, 42(3):272–278, 2002.
34. S R Stock. Recent advances in X-Ray microtomography applied to materials. *Int. Mat. Rev.*, 53(3):129–181, 2008.
35. T Taillandier-Thomas, S Roux, and F Hild. Soft route to 4D tomography. *Phys. Rev. Lett.*, 117:025501, 2016.
36. A Tarantola. *Inverse Problems Theory. Methods for Data Fitting and Model Parameter Estimation*. Elsevier Applied Science, Southampton (UK), 1987.
37. E.K. Tschegg. Equipment and appropriate specimen shapes for tests to measure fracture values. Austrian Patent Office, Patent AT-390328.
38. W. van Aarle, W. J. Palenstijn, J. De Beenhouwer, T. Altantzis, S. Bals, K. J. Batenburg, and J. Sijbers. The ASTRA toolbox: A platform for advanced algorithm development in electron tomography. *Ultramicroscopy*, 157:35–47, 2015.
39. E Verhulp, B van Rietbergen, and R Huiskes. A three-dimensional digital image correlation technique for strain measurements in microstructures. *J. Biomech.*, 37(9):1313–1320, 2004.